Seismic Evidence for a Crustal-scale Detachment Fault in the Woodlark Basin

Jacqueline S. Floyd*[1,2], John C. Mutter[1,2,3], and William H. Menke[1,2]

1. Department of Earth and Environmental Sciences, Columbia University, New York, NY, 10026.
2. Lamont-Doherty Earth Observatory, Columbia University, Palisades, NY, 10964.
3. Earth Institute, Columbia University, New York, NY, 10026.
*Corresponding author: jsfloyd@ldeo.columbia.edu.

Index terms: Seismology, Tectonophysics, Marine Geology and Geophysics, Exploration Geophysics, Structural Geology

Abstract

A combined land and marine three-dimensional seismic tomography study of the rifting-spreading transition in the western Woodlark Basin of Papua New Guinea reveals the deep structure of the rift zone and 'Moresby' detachment fault that divides the Woodlark and Pocklington Rises. The tomography study uses airgun shots from a 20 airgun, 10,850 cu. in. array aboard R/V *Maurice Ewing* that was shot at a rate of 100 s to an array of ocean bottom seismometers and hydrophones as well as PASSCAL seismometers installed at island stations around the rift zone. We achieved good signal-to-noise ratios at source-receiver ranges of up to 200 km with associated turning depths of up to ~35 km. The three-dimensional seismic velocity model images the 'Moresby' detachment fault that separates the northern and southern rift margins with good resolution to a depth of at least 15 km, where prior seismic reflection studies imaged the fault plane to only ~8-9 km below sea level. Beneath the inferred fault plane, we have also imaged a large, high-velocity body that we interpret to represent magmatic upwelling beneath the detachment, which is located less than 5 km west of the propagating tip of the Woodlark spreading center. These images support the hypothesis that the 'Moresby' detachment fault is in the final stages of transition from continental rifting to magmatic upwelling and seafloor spreading.

Text

The transition zone between continental rifting and seafloor spreading in the western Woodlark Basin of Papua New Guinea is one of the most rapidly extending rift zones known on Earth [*Taylor et al.*, 1995; *Abers*, 2001; *Baldwin et al.*, 2004]. The Woodlark spreading center is propagating westward into the northern Australian continental margin with a full spreading rate of ~3-4 cm/yr at its westernmost tip, located immediately east of Moresby Seamount [*Taylor et al.*, 1999] (Fig. 1) where it enters the rifting-spreading transition zone. Within the transition zone, lies a seismogenic [*Abers et al.*, 1997; *Abers*, 2001], shallowly-dipping normal fault that strikes westward from the spreading center tip to the region of continental rift initiation near the D'Entrecasteaux Islands (Fig. 1). Thus far, the fault has been imaged only to a depth of ~5-8 km by multichannel seismic reflection profiles and sampled by deep ocean drilling of the uplifted footwall known as Moresby Seamount [*Taylor and Huchon*, 2002]. Multichannel seismic reflection (MCS) profiles show that the 'Moresby' normal fault dips 25-30° to the north [*Mutter et al.*, 1993; *Abers et al.*, 1997]. Abers et al. (1997) proposed that a moment magnitude (M_w) 6.23 normal-faulting earthquake occurred on or near the fault at 5.3 km depth. The fault has been the subject of controversy because its dip lies near the 30° theoretical limit for frictional slip on normal faults [*Byerlee*, 1978; *Abers*, 2001], where fault mechanics favors the formation of a new normal fault rather than slip on an existing plane with unacceptably high friction. However, the recent discovery of a >4 m-thick layer of hydrothermally altered and serpentinized fault gouge on Moresby Seamount [*Shipboard Scientific Party*, 1999] and seismic reflection evidence for fluids

within the fault zone [*Floyd et al.*, 2001] suggest that the conditions for reducing friction on the fault plane may be present. High strain rates [*Abers*, 2001] at the rifting-spreading transition and high heat flow [*Floyd et al.*, 2001] from the advancing spreading center also have been proposed to provide favorable conditions for low-angle normal slip at this location. However, until now, there has not been evidence for a heat source beneath the fault plane.

We deployed an array of land and marine seismometers in and around the rifting-spreading transition of the Woodlark Basin to image the deep crustal structure of the rift zone and to record seismicity for analysis of active plate kinematics in the transition zone. A three-dimensional seismic velocity model based on airgun shots to the marine array was presented by Zelt et al. (2001). Here we combine data recorded by both the land and marine seismic arrays, which recorded refracted compressional (Pg) wave arrivals with much greater turning depths of up to 40 km. Using a tuned 10,800 cu. in., array of 20 airguns aboard the R/V *Maurice Ewing*, we fired a total of 3607 airgun shots spaced 100 s apart, or approximately 250 m at 4.5 kts. The airgun shots were recorded by seven Lamont Webb ocean bottom seismometers (OBS), seven Scripps L-Cheapo ocean bottom hydrophones (OBH), and nine PASSCAL seismometers installed at six sites on four of the islands surrounding the central rift zone. The ship's path and the seismometer locations are shown in Figure 1. Visually determined traveltime picking errors were estimated to be less than 45 ms. We identified a total of 49,180 first-arrival compressional-wave (Pg) seismic traveltimes for use in our tomographic inversion.

Three-dimensional (3D) velocity estimates for the rift zone were computed using compressional wave arrival times and 3D tomographic modeling code developed by

William Menke [*Menke*, 2004]. Our objective was to find a seismic velocity model for the rift zone that best predicts the first arrival compressional wave traveltimes from the airguns to the seismometers and hydrophones. We constructed a starting model in which the velocity varies only with depth, which we call the one-dimensional, or 1D, starting model, based on results of preliminary two-dimensional (2D) inversions located along several airgun shot lines. In addition, we referred to the seismic refraction results of Finlayson et al. (1976), who found a crustal thickness of ~25 km and an upper mantle velocity of 8.0 km/s in the northeast Papuan peninsula. The velocity model was calculated within a volume that is 225 km wide west to east, 265 km long north to south, and 60 km deep. The velocities are defined at grid nodes that sample the volume vertically every 2.5 km from the seafloor to 30 km depth, every 5 km between 30 and 40 km depth, and horizontally every 5 km in both east-west and north-south directions. The bottom layer of the model is placed at 60 km depth to ensure that traced rays, which were found to have a turning depth of less than 40 km, did not exit through the bottom of the model. The seismic ray coverage throughout the starting model is shown in Figure 2 as a function of the number of traversing rays that cross each velocity node. The best coverage area is located between 5 and 15 km depth. Nearby PASSCAL stations at Egum and Fergusson Island were not working during the shooting period resulting in a ray coverage pattern with an irregular boomerang shape.

We ran 1D inversions using every other airgun shot at ~500 m spacing to find the best-fitting 1D starting model and then ran three sets of 3D velocity inversions for damping parameter values of 0.1, 0.5, and 1.0 (see Methods). Three north-south oriented profiles through the final best-fit 3D velocity models are shown in Figure 4 and in

Supplementary Figures S2a and S2b. The velocity models show increasing structural variability with decreasing damping as expected. The results of the model with a damping of 0.1 are most consistent with the scale of structural resolution determined from checkerboard resolution tests (Fig. S1). Each model regardless of damping shows a large east-west trending, ~15-20° northward-dipping velocity contours north of Moresby Seamount and a high velocity body (>7.5 km/s) located beneath the rift axis. The north-dipping structure is located at the latitude of and parallel to the Moresby shallow-angle normal fault for at least 50 km along strike. We regard this structure as evidence for a crustal scale detachment. Northward-dipping velocity contours, which we infer to delineate the location of the detachment fault at depth, are easily identified near Moresby Seamount, but are less well resolved toward Normanby Island. While this is likely due in part to decreasing ray coverage to the west, this pattern is consistent with seismic reflection and bathymetric data, which suggest that the detachment forms a single boundary nearest the spreading center tip, and splays into one or more normal faults to the west toward Normanby Island (Fig. 2) [*Huchon et al.*, 2002]. The north-south cross-section that intersects Moresby Seamount (Fig. 4b) reveals a high-velocity (>7.0-7.5 km/s) structure that may be an isolated body (Fig. 4b,c) or that may extend down to the mantle (Fig. 4a) below the depth extent of our ray coverage. We interpret the body to represent mantle upwelling, which would be expected to present in the propagation path of the westernmost Woodlark spreading center segment.

Initial attempts to constrain the crustal thickness in this area from 2D refraction profiles met with limited success due to the shallow penetration depth of Pg arrivals to the seafloor stations in the center of the study area, making it impossible to reverse the

30-40 km-deep turning rays recorded by the land stations. Finlayson et al. [*Finlayson et al.*, 1976] estimated a crustal thickness of 23.7 km beneath the Trobriand Platform (Fig. 1), while Abers et al. [*Abers*, 2001] found crustal thicknesses of 20-30 km using receiver function estimates from land stations on the nearby islands (Fig. 1). These thicknesses are greater than our 15 km limit. Velocities of more than 7 km/s at shallow (<10 km) depths beneath the rift axis and immediately north of Moresby Seamount suggest that the shallow, lower seismic velocity crust has thinned and that associated mantle upwelling has occurred beneath the rift axis north of Moresby Seamount. The crust may also thin south of Normanby Island and Moresby Seamount, but these regions are not well constrained. High velocities of 7.0-7.5 km/s are observed just under Normanby Island, but we cannot determine whether these are connected to deeper levels of the crust given the limited ray coverage in this area.

The 3D seismic tomography images reveal several new features in the rifting-spreading transition of the western Woodlark Basin. Perhaps most importantly, the new images of the rift axis north of Moresby Seamount suggest that the 'Moresby' normal fault descends into the mid-crust to at least 15 km depth and defines the newly forming tectonic plate boundary west of the Woodlark spreading center. We estimate a dip of 15-20° for this structure, which is significantly less than the 25-30° estimated for the upper ~5 km of the normal fault imaged in seismic reflection profiles, suggesting that the fault may flatten with depth. We suggest that the high velocity body observed in the mid-crust north of Moresby Seamount represents mantle upwelling ahead of the propagating spreading center (Fig. 4). Although we cannot fully resolve the depth extent of this feature, we propose that it is continuous with the mantle beneath and that it penetrates to

mid-crustal levels along the detachment. Hence, we suggest that the detachment must penetrate to mantle depths also.

Our tomographic images thus reveal a major crustal detachment that is continuous with the 'Moresby' normal fault that is known to exist at shallow levels from multichannel seismic reflection profiles and deep-ocean drilling. The high velocity feature just west of the spreading center and below the detachment is best interpreted as a mantle body and is critical to establishing the velocity structure of the detachment at depth. We note that in older rift settings where a mantle body is not or is no longer present, it may be difficult to detect detachment faults in the mid-crust because there is not enough contrast in seismic velocity and density across the fault plane. This could explain why seismic images of large-scale crustal detachments have proven elusive in old passive margins.

Supporting Material

Methods

Waterwave traveltimes were used to relocate the OBSs on the seafloor using a one-dimensional velocity model for the water column, which was calculated from expendable bathymetry thermograph (XBT) measurements collected during the September 1999 cruise. All of the instruments recorded continuously with sampling rates of 15.625 ms (64 Hz) for the OBSs, 8 ms (125 Hz) for the OBHs, and 20 ms (50 Hz) for the PASSCAL seismometers. The OBSs recorded continuously from September 1999 to February 2000. The land stations were deployed for an overlapping period from July 1999 to June 2000 as part of the earthquake monitoring experiment[*Mutter et al.*, 2000]. Clock corrections were applied to all of the stations except OBSs Helmut and Salote due to instrument malfunctions. We used teleseismic compressional-wave arrival times to the OBSs to estimate clock drifts and found a drift of 398.0±216 ms (3.6 ms/day) for OBS Helmut and 712.3±208.8 ms (6.4 ms/day) for OBS Salote. These estimated clock drift values are in good agreement with the average drift of 500 ms calculated for all of the OBSs.

We performed resolution tests to determine the ability of the 3D model to resolve features on the scale of 10 km in the crust, which is twice the average OBS spacing (Fig. S1). The model resolution at any point is a function of the number of crossing rays through the point as well as the relative raypaths orientations determined by source-receiver azimuths. We placed 10x10 km positive and negative velocity anomalies of ±0.75 km/s in a three-dimensional checkerboard pattern within the volume. The model was filtered in three-dimensions to smooth the edges of the anomalies and prevent ray

loss. We then calculated traveltimes for rays passing through the model with the same source-receiver configuration as that used in our experiment. Starting with the best-fit 1D model, we ran six iterations to recover the checkerboard velocity anomaly pattern. As may be anticipated from the ray coverage plots (Fig. 2), the best resolution is found at around 10 km depth, where the checkerboard pattern is best recovered by the inversion (Fig. S1a). Velocity perturbations at depths greater than 10-15 km and along the outer paths to the land stations smear in the direction of the ray paths and have poor resolution due to lack of full azimuthal coverage. These results place limits on our ability to accurately recover structures below these depths in the 3D inversion.

Damping was used to limit the magnitude of the velocity perturbations that were calculated for each iteration. Higher damping values preserved more traced rays at the expense of creating an overly smooth model [*Menke*, 2004]. We tested inversion damping parameters over three orders of magnitude between 0.1 and 10.0. A high damping value of 10.0 produced very small perturbations relative to the 1D starting model. Damping values of 0.1 or less produced spurious velocity anomalies and overly complex velocity models that did not appear to be geologically reasonable. The damping values that produced the most reasonable results ranged between 0.1 and 1.0. We ran nine iterations of the tomographic inversion for damping values of 0.1, 0.5, and 1.0. The root-mean-squared (RMS) traveltime reduction, number of traced rays, and processing time for each iteration are plotted in Figure S4. Approximately 85% of the total RMS traveltime error reductions were produced in the first three iterations (Fig. S4a). Smaller damping values produced smaller RMS traveltime errors; however, as shown in Figure A4b, these resulted in larger velocity perturbations and reduced the total number of rays

that could be traced between the sources and receivers. The processing time, which scales with the number of traced rays, decreased as rays were lost with each iteration (Fig. S4b).

Acknowledgments

This work was supported by NSF Grant #0118568.

Reference List

Abers, G.A., Evidence for seismogenic normal faults at shallow dips in continental rifts, in *Non-volcanic Rifting of Continental Margins: A Comparison of Evidence from Land and Sea*, edited by R.C.L. Wilson, R.B. Whitmarsh, B. Taylor, and N. Froitzheim, pp. 305-318, Geological Society, London, 2001.

Abers, G.A., C.Z. Mutter, and J. Fang, Shallow dips of normal faults during rapid extension: Earthquakes in the Woodlark-D'Entrecasteaux rift system, Papua New Guinea, *Journal of Geophysical Research*, *102* (B7), 15301-15317, 1997.

Baldwin, S.L., B.D. Monteleone, L.E. Webb, P.G. Ritzgerald, M. Grove, and E.J. Hill, Pliocene eclogite exhumation at plate tectonic rates in eastern Papua New Guinea, *Nature*, *431*, 263-267, 2004.

Byerlee, J.D., Friction of rocks, *Pure and Applied Geophysics*, *116*, 615-626, 1978.

Finlayson, D.M., K.J. Muirhead, J.P. Webb, G. Gibson, A.S. Furumoto, R.J.S. Cooke, and A.J. Russell, Seismic investigation of the Papuan Ultramafic Belt, *Geophy. J. of the Royal Astron. Soc.*, *44*, 45-59, 1976.

Floyd, J.S., J.C. Mutter, A.M. Goodliffe, and B. Taylor, Evidence for fault weakness and fluid flow within an active low-angle normal fault, *Nature*, *411*, 779-783, 2001.

Huchon, P., B. Taylor, and A. Klaus, Procs. ODP, Sci. Res., pp. [CD-ROM], ODP/TAMU, College Station, 2002.

Menke, W., Case studies of seismic tomography and earthquake location in a regional context, in *Seismic Data Analysis and Imaging with Global and Local Arrays*, edited by A. Levander, and G. Nolet, pp. in press, American Geophysical Union, 2004.

Mutter, J.C., J.S. Floyd, A. Lerner-Lam, B. Taylor, G. Abers, and A. Ferris, Active and natural seismicity investigation of continental breakup in the western Woodlark Basin, *Eos, Transactions AGU*, S414, 2000.

Mutter, J.C., C.Z. Mutter, G.A. Abers, and J. Fang, Seismic images of low-angle normal faults in the western Woodlark Basin where continental extension yields to seafloor spreading, *Eos, Trans. AGU*, *74*, 412, 1993.

Party, S.S., Leg 180 Summary, in *Proc. ODP, Init. Repts.*, edited by B. Taylor, P. Huchon, A. Klaus, and S.S. Party, pp. 1-77, Ocean Drilling Program, College Station, TX, 1999.

Taylor, B., A. Goodliffe, F. Martinez, and R. Hey, Continental rifting and initial seafloor spreading in the Woodlark Basin, *Nature*, *374* (6522), 534-537, 1995.

Taylor, B., A.M. Goodliffe, and F. Martinez, How continents break up: Insights from Papua New Guinea, *Journal of Geophysical Research*, *104*, 7497-7512, 1999.

Taylor, B., and P. Huchon, Active continental extension in the western Woodlark Basin: a synthesis of Leg 180 results, in *Proceedings of the Ocean Drilling Program, Scientific Results*, edited by P. Huchon, B. Taylor, and A. Klaus, pp. 1-36 [CD-ROM], Ocean Drilling Program, College Station, TX, 2002.

Zelt, B.C., B. Taylor, and A.M. Goodliffe, 3-D crustal velocity structure at the rift tip in the western Woodlark Basin, *Geophysical Research Letters*, *28* (15), 3015-3018, 2001.

Figure Captions

1. Topographic map of the western Woodlark Basin showing the location of the R/V *Maurice Ewing* airgun shot lines (black lines), OBSs (white squares) and OBHs (white triangles), and PASSCAL stations (white and gray circles). PASSCAL stations that were inoperable during the active source experiment are marked with gray circles.

2. Ray density map showing the number of crossing rays penetrating each velocity node in the 3D model volume at 5, 10, 15, and 20 km depth. Rays to the marine array reach up to ~15 km depth, while rays to the PASSCAL stations reach further than 20 km depth.

3. Map view of the area enclosed by the 3D velocity model volume in a Cartesian coordinate system in units of kilometers. Triangles mark receiver locations. The locations of the 3D model cross-sections in Figure 4 are shown by black lines A-C.

4. North-south oriented cross-sections from the final 3D tomographic velocity model for a damping parameter value of 0.1. (Cross-sections of the model for damping parameter values of 0.5 and 1.0 are shown in Figures S2 and S3.) Refer to Figure 3 for the profile locations. The dashed white line in 4C shows the inferred location of the detachment fault north of Moresby seamount. We interpret the body marked by the 7.5 km/s isovelocity contour to indicate mantle upwelling.

Figure Captions for Supplementary Material

S1. Resolution test results for a 3D checkerboard-pattern velocity model with ±0.075 km/s velocity perturbations at depths of 5 and 15 km. The bottom row shows the synthetic checkerboard velocity pattern for depths (Z) of 5 and 15 km, while the top row shows the recovered velocity perturbation model outlined by the limit of the ray coverage (black line). The velocity layers within the model are draped from the seafloor, creating lateral variations observed at Z = 15 km.

S2. North-south oriented cross-sections from the final 3D tomographic velocity model for a damping parameter value of 0.5. Refer to Figure 3 for the locations of the profiles.

S3. North-south oriented cross-sections from the final 3D tomographic velocity model for a damping parameter value of 1.0. The higher damping value limits perturbations from the starting model, resulting in a smoother result with lower resolution. Refer to Figure 3 for the locations of the profiles.

S4. (A) Percent root-mean-squared (RMS) traveltime error reduction (solid lines), and starting RMS traveltime error (solid dots) for each iteration. Plot A shows that error reduction did not improve significantly after the fourth iteration. (B) Number of rays traced through the model (solid lines) and the computing (CPU) time for each iteration. The computing time decreased as the number of traced rays decreased with each successive iteration.

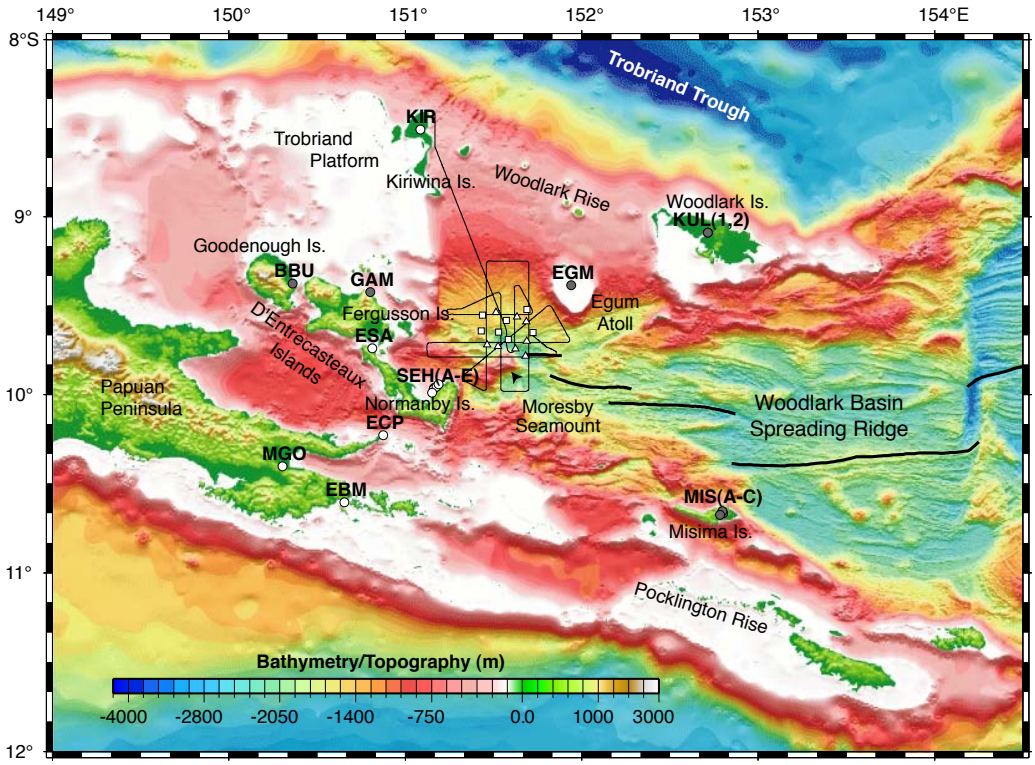

Floyd et al., Figure 1.

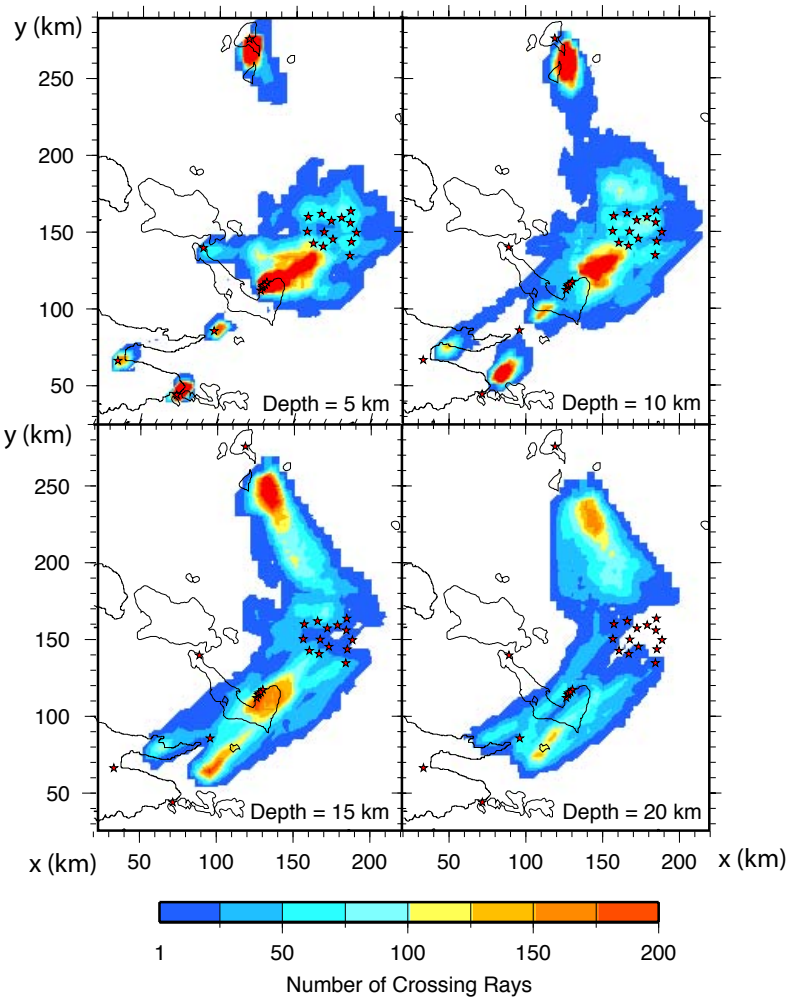

Floyd et al., Figure 2.

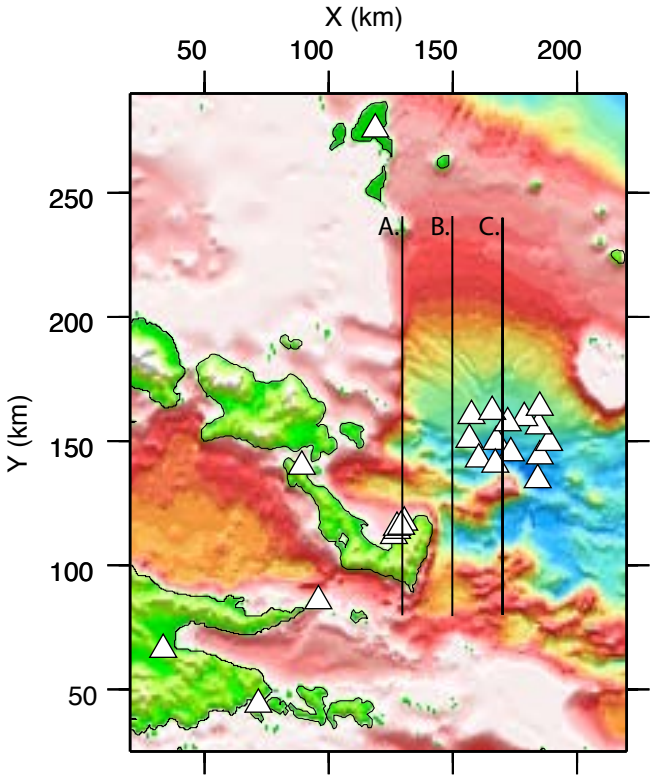

Floyd et al., Figure 3.

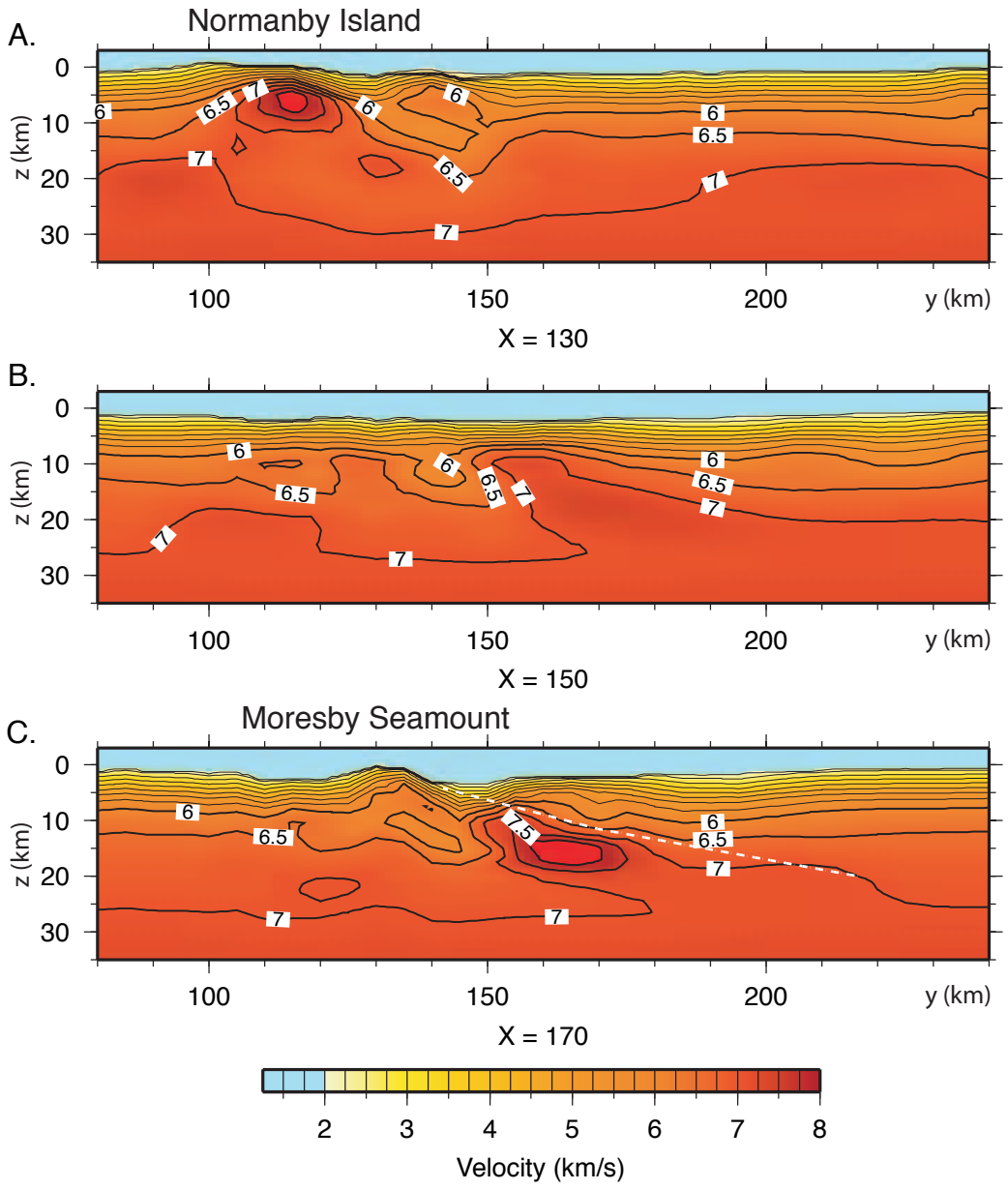

Floyd et al., Figure 4.

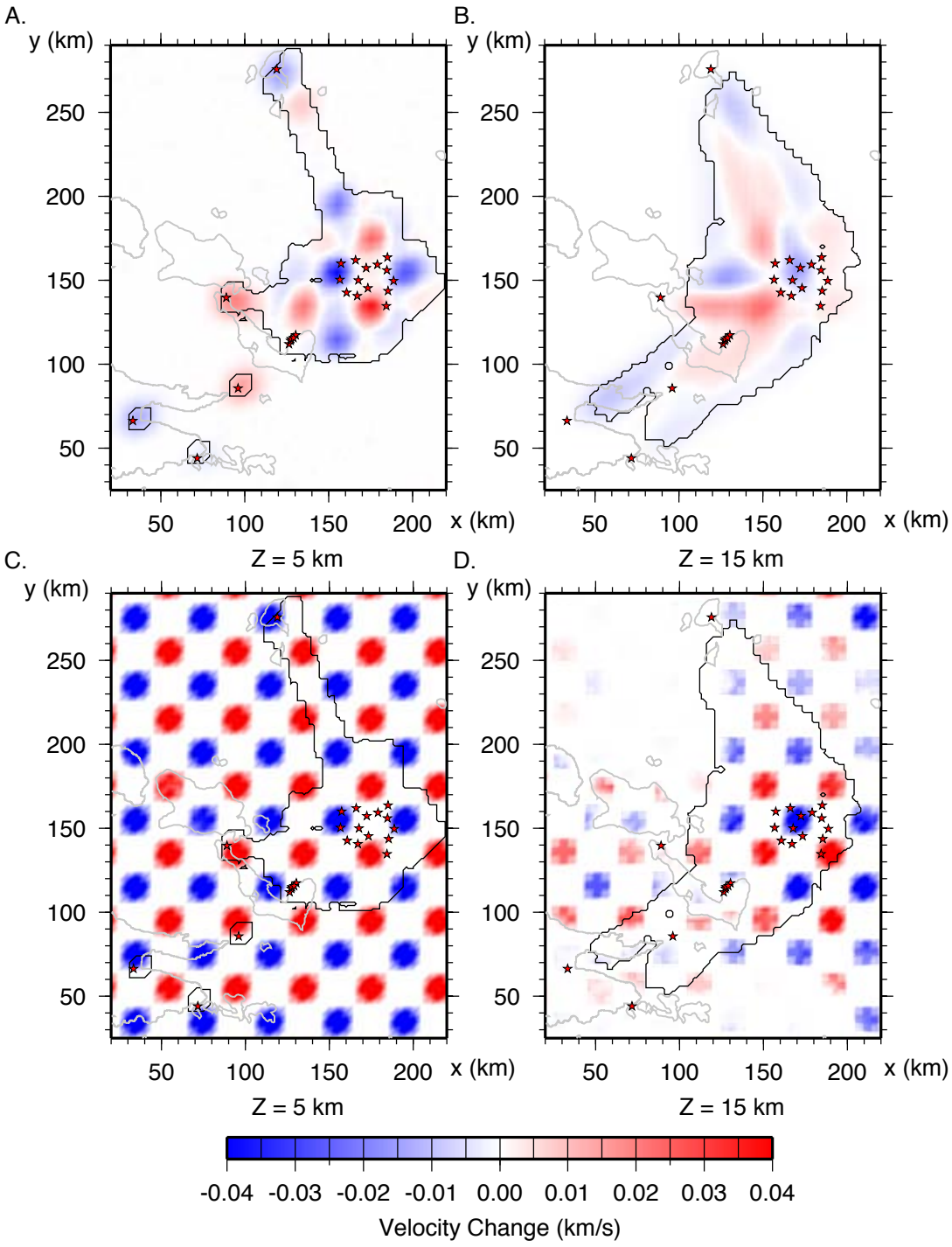

Floyd et al., Figure S1.

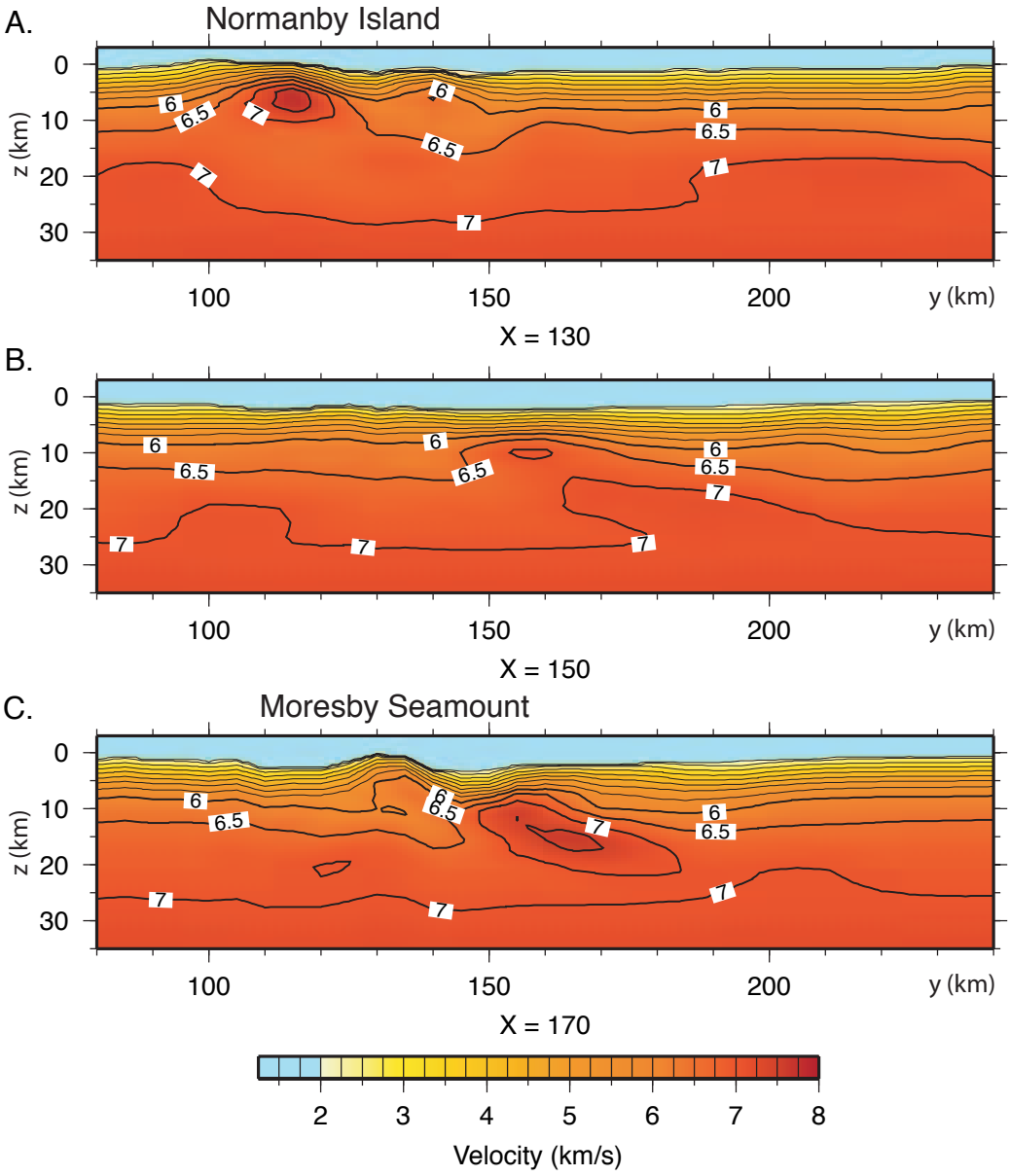

Floyd et al., Figure S2.

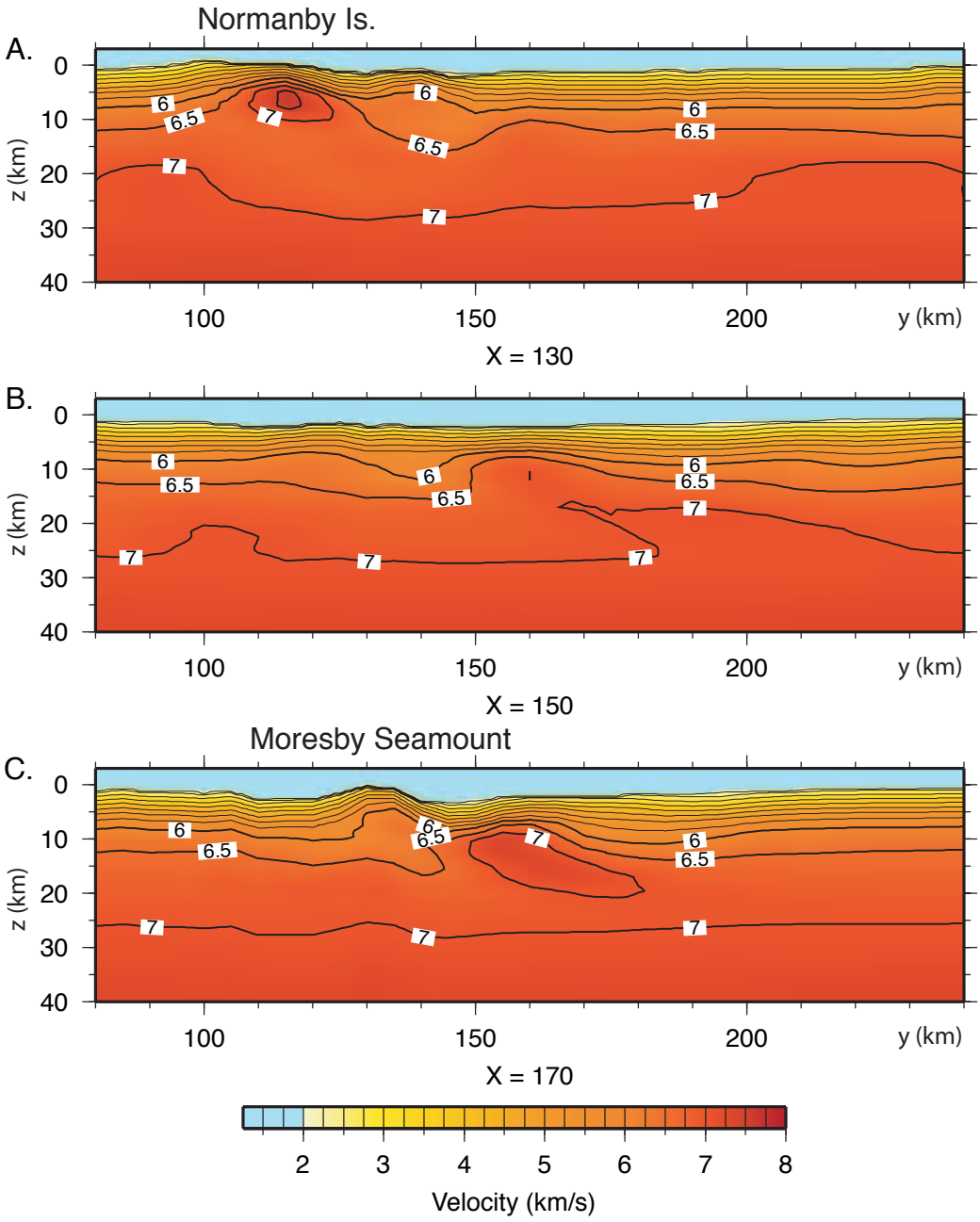

Floyd et al.,, Figure S3.

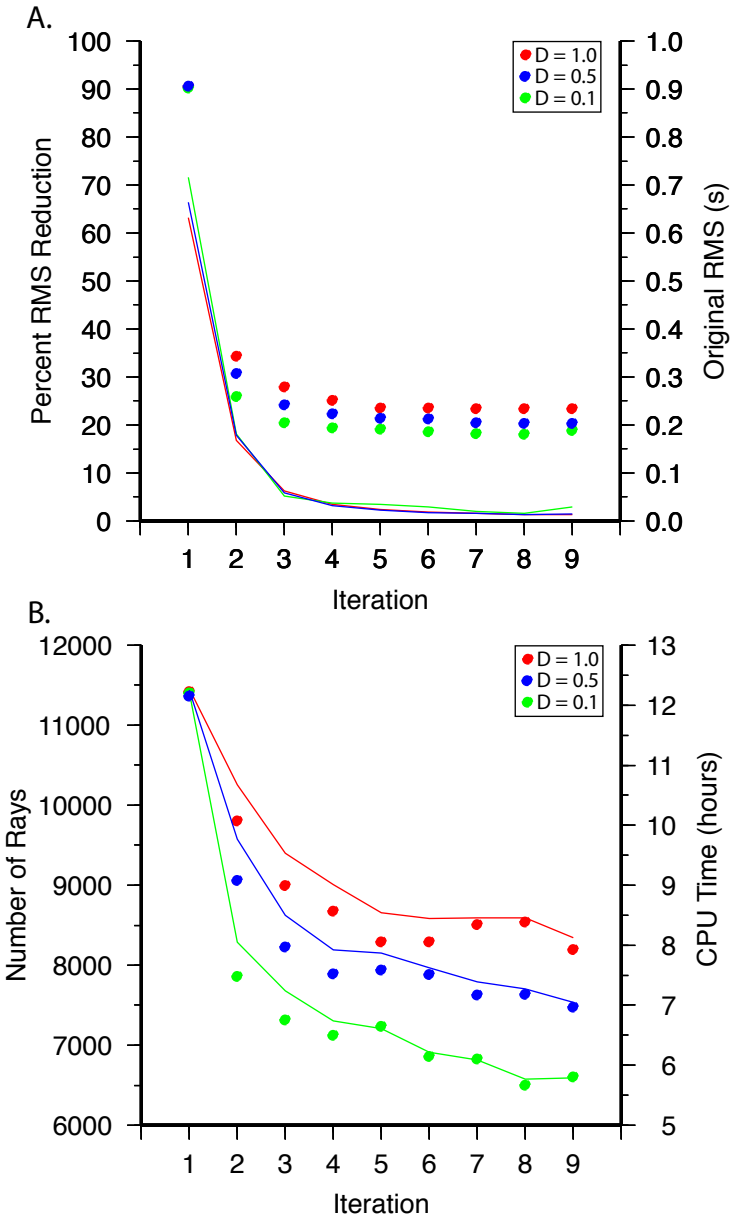

Floyd et al., Figure S4.